

Discrepancy in parameter constraints for LTB models using BAO and SNIa

C Z Vargas¹, F T Falciano¹ and R R R Reis^{2,3}

¹ Centro Brasileiro de Pesquisas Físicas, Rua Xavier Sigaud st. 150, 22290-180, Rio de Janeiro, Brazil

² Instituto de Física, Universidade Federal do Rio de Janeiro, Av. Athos da Silveira Ramos 149, 21941-972, Rio de Janeiro, RJ, Brazil

³ Observatório do Valongo, Universidade Federal do Rio de Janeiro, Ladeira do Pedro Antônio 43, CEP 20080-090 Rio de Janeiro, RJ, Brazil

E-mail: czuniga@cbpf.br, ftovar@cbpf.br and ribamar@if.ufrj.br

Received 30 March 2016, revised 5 October 2016

Accepted for publication 10 November 2016

Published 20 December 2016



Abstract

In the present work we constrain three different profiles of a Lemaître–Tolman–Bondi model using supernovae type Ia and baryon acoustic oscillation data. We use two distinct parameter estimation approaches, namely, the χ^2 and the complete Likelihood functional. It has been argued that these two approaches are not equivalent and indeed our analysis shows a specific example of their departure. The combined analysis of BAO + SNIa offers a stringent test for these models. In addition, we improve common practice in the literature by carefully calibrating the supernovae in the appropriate inhomogeneous background dynamics. We address subtle issues in order to propagate the primordial BAO scale to the present epoch.

Keywords: baryon acoustic oscillations, type Ia supernovae, LTB model

(Some figures may appear in colour only in the online journal)

1. Introduction

At the turn of the last century, observations of distant supernovae type Ia (SNIa) [1, 2] together with the observation of the cosmic microwave background [3] and the large-scale structure [4–7] led us to consider that the universe could be accelerating. In the framework of a Friedmann–Lemaître–Robertson–Walker (FLRW) universe, the source for this acceleration has to be an exotic component dubbed dark energy. The simplest dark energy alternative is to include a constant term in the dynamic equations, which indeed is how the current concordance model describes dark energy, i.e. as a cosmological constant. As is well-known, the Λ CDM model is successful in accommodating much observational data within a single

consistent scenario. Notwithstanding, there are still open issues that challenge the Λ CDM model from an observational point of view (see [8] for a recent review).

Despite the cosmological constant, that arguably displays from theoretical inconsistency, there are several other candidates for dark energy such as quintessence fluids [9], K-essence [10] and Chaplygin gas [11] just to name a few. There is also the possibility of mimicking dark energy by modifying the gravitational interaction. In these scenarios one changes General Relativity for other theories like $f(R)$ theories [12], DBI Galileons [13] or Brane world cosmology [14] that produce an early or late time accelerating expansion of the universe.

Within the scope of general relativity (GR), there are two possible routes to induce the present acceleration. The first is to consider phenomenological averaging approaches that explore the fact that smoothing does not commute with GR dynamics and hence smoothing spacetime on cosmological scales and then evolving through Einstein's equations should give a different result as to using the full dynamics and then smoothing at the end (see [15] for observational constraints).

The other possibility is to revoke the Copernican Principle (CP), hence one can construct inhomogeneous models that can suppress the need for dark energy [16–19]. Their validity relies on the underdetermination of the model from observational data. Our data comes only from our past null cone and hence there is a collection of geometries compatible with the observational data. These models are effective with inhomogeneities of the order of a few fractions of the Hubble radius. However, they are not effective to simultaneously explain all datasets available today. In particular, the Kinematic Sunyaev–Zel'dovich (kSZ) effect is very stringent and a powerful probe of inhomogeneities since it carries information not only from the light-cone but also within it. With mild assumptions one can show that, even with their extra degrees of freedom, LTB models will hardly be able to incorporate simultaneously all the observational datasets [20–22]. Notwithstanding, LTB can still be interesting exact solutions to probe the impact of inhomogeneities on observational data [23–25].

In a FLRW model the dynamics is entirely encoded in the scale factor. In inhomogeneous models, the spatial dependence gives extra degrees of freedom, which in principle could better accommodate the data. Thus, it seems critical to have at least two independent observations to restrict inhomogeneous models. It is expedient that the number of free parameters of each model should be as low as possible and the number of independent observations as high as possible. In particular, in this paper we use the joint light-curve analysis sample [26] known as the JLA sample. This extended sample of 740 supernovae combines low-redshift samples ($z < 0.1$), the third year Sloan Digital Sky Survey sample (SDSS-II, $0.05 < z < 0.4$), the third year SuperNova Legacy Survey (SNLS, $0.2 < z < 1$) and the Hubble space telescope sample (HST, $z > 1$).

The goal of this article is to implement a comparative analysis using two different statistical approaches of the best fit of inhomogeneous models using SNIa and baryon acoustic oscillation (BAO) data. We test the validity of the χ^2 minimization method as compared to the extremization of the Likelihood functional. It has been argued that these two approaches are not equivalent and indeed our results show a concrete example of their departure. The breakdown of the χ^2 minimization is rooted in the dependence of the normalization factor of the Likelihood functional with the nuisance parameters in the supernovae distance modulus.

We consider three different profiles of a Lemaître–Tolman–Bondi (LTB) model of the universe. Contrarily to some analysis in the literature, we carefully calibrate the SNIa data for an LTB dynamics. In an LTB universe, there are also subtle adjustments to propagate the primordial BAO scale to the present epoch. The combined analysis of BAO + SNIa offers a stringent test for the models presented in this article.

The paper is organised as follows. In the next section we briefly review the main points of an LTB model and its dynamics. In section 3 we specify the inhomogeneous matter profiles and in section 3.2 we describe how to incorporate the BAO physics in an LTB dynamics. In section 4 we characterize the SNIa and BAO data used to fit the models and discuss the results in section 5. Section 6 is reserved for final comments and conclusions.

2. The LTB model

The standard cosmological model describes our universe being on average homogeneous and isotropic where the background is assumed to be a FLRW metric. This is the mathematical formulation of the cosmological principle which is a possible way to implement the Copernican principle, namely, the statement that we are not in a privileged location in the universe. For most of the last century, homogeneity and isotropy were only valuable assumptions but recently it has been shown they are consistent with observation (if one accepts the existence of dark energy and dark matter). Even though there is no direct confirmation of spatial homogeneity, observational data does support spatial isotropy with respect to our point of observation [15].

In the present work we shall drop homogeneity but still maintain the isotropy condition. Thus, the observable universe will be modeled by an inhomogeneous but spherically symmetric metric, which we assume to be of the LTB type [27–29]. This family of metrics can be written⁴ as

$$ds^2 = dt^2 - \frac{X'^2(t, r)}{1 + 2E(r)} dr^2 - X^2(t, r) d\Omega^2. \quad (1)$$

where $d\Omega^2 = d\theta^2 + \sin^2\theta d\varphi^2$ is the solid angle and prime denotes partial derivatives with respect to the radial coordinate, i.e. $X' = \partial_r X$. The energy function $E(r)$ can be related to the non-constant spatial curvature and $X(t, r)$ plays the role of a scale function that can depend both on time and radial coordinates. It is straightforward to check that (1) reduces to an FLRW metric when $X(t, r) = a(t)r$ and $2E(r) = -\kappa r^2$ with $\kappa = 0, \pm 1$.

The LTB metric (1) has two effective scale factors, namely, the transverse or angular scale factor $X(t, r)$ which is associated with the area radius of each S^2 sphere and the parallel or radial scale factor $X'(t, r)$. Thus, contrasting to the FLRW metric, which has only one Hubble factor, it is convenient to define two Hubble parameters

$$H_{\perp}(t, r) \equiv \frac{\dot{X}(t, r)}{X(t, r)} \quad \text{and} \quad H_{\parallel}(t, r) \equiv \frac{\dot{X}'(t, r)}{X'(t, r)}, \quad (2)$$

that represent, respectively, the transverse and radial expansion rates. The dots in the above equation denote partial derivatives with respect to time coordinates, i.e. $\dot{X} = \partial_t X$. It is also possible to define a geometrical mean out of these Hubble parameters as

$$\bar{H}_{\text{LTB}}(t, r) = [H_{\parallel}(t, r) H_{\perp}^2(t, r)]^{1/3}. \quad (3)$$

The matter content is described by a pressureless inhomogeneous fluid whose stress-energy tensor can be written as $T^{\mu\nu} = \rho(t, r)u^{\mu}u^{\nu}$, where u^{μ} is the four-velocity field of the fluid. Due to the symmetries of (1), the analogue Friedmann-like equation reads

$$H_{\perp}^2 - \frac{2E}{X^2} = \frac{2M}{X^3}, \quad (4)$$

⁴ Units in which $c = 1$ will be assumed in the following.

where $M(r)$ is another free function of r that can be interpreted as the gravitational mass inside a spherical shell of radius r . This mass function is connected to the energy density through the relation

$$\rho(t, r) = \frac{1}{8\pi G} \frac{M'}{X^2 X'} \quad (5)$$

Equations (4) and (5) compose the dynamic field equations for a dust LTB spacetime. The time derivative of (5) combined with (4) implies a continuity equation for the energy density

$$\dot{\rho}(t, r) + (2H_{\perp} + H_{\parallel})\rho(t, r) = 0. \quad (6)$$

The above equation prompts us to define another mean Hubble factor through an arithmetic mean as

$$\langle H \rangle(t, r) = \frac{1}{3}(2H_{\perp} + H_{\parallel}). \quad (7)$$

The analogy between an LTB model and an FLRW universe can be carried further by defining a dimensionless matter and curvature density parameters evaluated today given, respectively, as

$$\Omega_M(r) = \frac{2M(r)}{H_{\perp 0}^2(r)X_0^3(r)} \quad \text{and} \quad \Omega_K(r) = \frac{2E(r)}{H_{\perp 0}^2(r)X_0^2(r)}. \quad (8)$$

Note that equation (4) means that these two density parameters are related by $\Omega_M(r) + \Omega_K(r) = 1$. Additionally, labeling the present values of the Hubble factor and the scale function, respectively, as $H_{\perp 0}(r) \equiv H_{\perp}(t_0, r)$ and $X(t_0, r) \equiv X_0(r)$, we can recast (4) as [30, 31]

$$H_{\perp}^2(t, r) = H_{\perp 0}^2(r) \left[\Omega_M(r) \left(\frac{X_0(r)}{X(t, r)} \right)^3 + \Omega_K(r) \left(\frac{X_0(r)}{X(t, r)} \right)^2 \right]. \quad (9)$$

The main difference from the homogeneous Friedmann equation is that LTB generalization (9) has space and time dependence. All the LTB quantities depend not only on time but also on the radial coordinate r . Notwithstanding, the whole formalism is covariant under radial coordinate re-definition. Indeed, the LTB metric (1) and all the formulae are covariant under the change $r \rightarrow f(r)$. Therefore, by a suitable choice of radial coordinate one can choose freely the value of the scale function today $X_0(r)$. A convenient choice that will be assumed in what follows is $X_0(r) = r$. This gauge fixation is similar to the normalization of the scale factor today for an FLRW universe, i.e. choosing $a(t_0) = 1$.

The Friedmann-like equation (9) can be integrated to give the age parameter $\Delta t(r)$. The spatial inhomogeneity of the metric induces a spatial dependent age parameter. It is convenient to fix the age parameter as the time spanned since the Big Bang time $t_B(r)$ which is defined as the time when $X(t_B, r) = 0$. Thus, integrating (9) gives

$$\Delta t(r) = t - t_B(r) = \frac{1}{H_{\perp 0}(r)} \int_0^{x(t, r)} \frac{dy}{\sqrt{y^{-1}\Omega_M + \Omega_K}}, \quad (10)$$

where $x(t, r) = X(t, r)/X_0(r) = r^{-1}X(t, r)$. The Big Bang time works as a constant of integration and as such is a free function of the model. The model is formally specified once the matter density parameter $\Omega_M(r)$ and the Big Bang time $t_B(r)$ are given. In principle one could choose arbitrarily these two functions at each spatial location. However, it has been

shown [32, 33] that even a small spatial dependence on the Big Bang time can produce too large inhomogeneities today to agree with the observed CMB. Thus, we commonly assume a simultaneous Big Bang time such that $t_B(r) = t_*$ with t_* a constant. With the hypothesis of a simultaneous Big Bang, the numerical value of t_* is not important and we can set it to zero. Equation (10) calculated today gives

$$H_{\perp 0}(r) = \frac{1}{t_0} \int_0^1 \frac{dy}{\sqrt{y^{-1}\Omega_M + \Omega_K}}, \quad (11)$$

where t_0 is the age of the universe which is chosen to be $t_0 = 13.7$ Gyr.⁵ Note that $H_{\perp 0}(r)$ is measured in units of Gyr^{-1} . For each Ω_M , equation (11) allows us to calculate the Hubble factor today $H_{\perp 0}(r)$ which then can be used in (9) to generate the scale factor $X(t, r)$ and all its derivatives for each radius and time.

The above procedure yields the background dynamics. In order to compare the LTB model with observations, we also need to construct the light paths. This is accomplished by solving the appropriate null geodesics for the model. The LTB spacetime is spherically symmetric which implies that an observer at its center of symmetry ($r = 0$) will measure incoming radial trajectories. Thus, we can consider with full generality radial geodesics to follow a line with $d\theta = d\varphi = 0$. The null geodesics has a vanishing interval, i.e. $ds^2 = 0$, hence, (1) show us that for null geodesics we have

$$\frac{dt}{d\lambda} = -\frac{dr}{d\lambda} \frac{X'(t, r)}{\sqrt{1 + 2E(r)}}, \quad (12)$$

where λ is an affine parameter and we kept the minus sign inasmuch we are considering incoming trajectories. It can be shown [31] that for two successive light rays, obeying the above radial null geodesic and emitted, respectively, at time t_1 and $t_1 + \delta t$, the period between wavefronts satisfies

$$\frac{d\delta t}{d\lambda} = -\frac{dr}{d\lambda} \frac{\dot{X}'(t, r)\delta t(\lambda)}{\sqrt{1 + 2E(r)}}. \quad (13)$$

Recalling the redshift definition, namely $z(\lambda) = \nu_0/\nu(\lambda) - 1$, (13) can be recast as

$$\frac{dz}{d\lambda} = (1 + z) \frac{dr}{d\lambda} \frac{\dot{X}'(t, r)}{\sqrt{1 + 2E(r)}}. \quad (14)$$

Equations (12) and (14) determine the null geodesic equations in terms of the redshift

$$\frac{dt}{dz} = -\frac{X'(t, r)}{(1 + z)\dot{X}'(t, r)}, \quad (15)$$

$$\frac{dr}{dz} = \frac{c\sqrt{1 + 2E(r)}}{(1 + z)\dot{X}'(t, r)}, \quad (16)$$

where we have explicitly re-introduced the speed of light $c \approx 0.3$ Gpc Gyr^{-1} .⁶

⁵ Comparing to the best fit ΛCDM model, that corresponds to fix $H_0 = 71$ Km Mpc^{-1} s^{-1} .

⁶ Note that writing the speed of light in units of Gpc Gyr^{-1} we obtain the luminosity distance in Gpc since we have set our time scale in Gyr.

In order to solve (15) and (16) we need two initial conditions. A suitable choice is the point at $z = 0$ given by $(t(0) = t_0, r(0) = 0)$. Thus, solving the system (15) and (16) we have the light curve $(t(z), r(z))$.

In an LTB universe, the angular diameter distance measured by an observer at the center is directly related to the scale function. With the procedure described above, we have the scale function at every point $X(t, r)$ and the radial null trajectory $(t(z), r(z))$, hence, we can follow the scale function throughout the geodesics and obtain the angular diameter distance as a function of the redshift

$$d_A^{\text{LTB}}(z) = X(t(z), r(z)). \quad (17)$$

In addition, we can also calculate the luminosity distance directly through its relation with the angular diameter distance [34, 35], namely

$$d_L^{\text{LTB}}(z) = (1 + z)^2 d_A^{\text{LTB}}(z). \quad (18)$$

Finally, in order to relate the inhomogeneous LTB model with the SNIa observations we also need the distance modulus

$$\mu_{\text{th}}^{\text{LTB}}(z) \equiv m - M = 5 \log_{10} \left(\frac{d_L^{\text{LTB}}(z)}{10 \text{ pc}} \right), \quad (19)$$

where m is the apparent magnitude of a source with absolute magnitude M . For every matter density profile $\Omega_M(r)$ we can run the above scheme and fit the observational data.

3. The void profiles

As is well known, in the Λ CDM model the observed dimming of distant supernovae can only be explained by the ad hoc hypothesis of a dark energy component responsible for driving the recent accelerating expansion of the universe. However, within spherically symmetric inhomogeneous models, it is possible to generate the observed dimming of distant objects via a local underdense region.

In the present work, we analyze three different profiles of matter distributions, namely the CGBH, Gaussian-like and the $C\nu$ -ln2 profile which we describe below. All three profiles share two main properties. They describe a local spherically symmetric underdense vicinity that smoothly approaches unity in the faraway region (see figure 1). The parameters of each profile are chosen such as to recover asymptotically the FLRW spacetime. This asymptotic behaviour also guarantees that in the far past all models approach an FLRW universe.

In [36], Garcia-Bellido and Haugbølle proposed a model with six parameters that is completely characterized by the matter density $\Omega_M(r)$ and the transverse expansion rate today $H_{\perp 0}(r)$. Their parameterization fixes the inner and outer values of Ω_M and $H_{\perp 0}$ and also how large and smooth is the transition from the inner and outer regions. They have also considered a more constrained profile (CGBH) by requiring a simultaneous Big Bang time. This extra condition imposes a relation between the expansion rate and the matter density and hence this model has only a single free function.

The CGBH profile can be parameterized as

$$\Omega_M(r) = \Omega_{M\text{out}} + (\Omega_{M\text{in}} - \Omega_{M\text{out}}) \left[\frac{1 - \tanh[(r - r_0)/2\Delta r]}{1 + \tanh(r_0/2\Delta r)} \right], \quad (20)$$

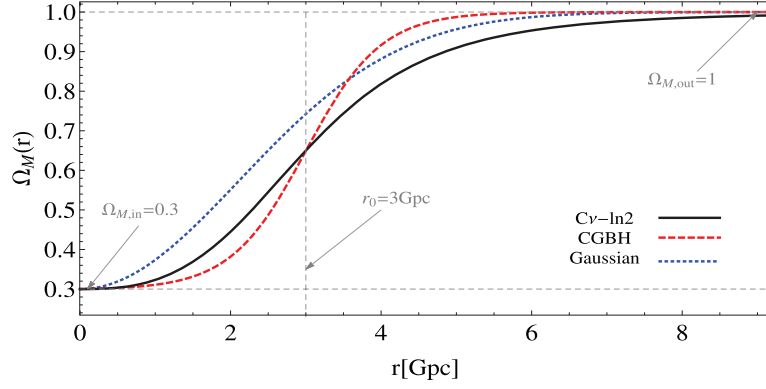


Figure 1. Matter density parameter today as a function of the radial coordinates. In all three profiles the outer density parameter is chosen to be unity, $\Omega_{M,\text{out}} = 1$. The others are free parameters to be adjusted with observational data. To plot the profiles we used $\Omega_{M,\text{in}} = 0.3$, $\Delta r = \nu = 0.5$ and $r_0 = 3$.

where $\Omega_{M,\text{in}}$ is the matter density at the center of the void and r_0 is the typical size of the void. The Δr parameter controls the steepness of the transition from inside to outside the void. In order to well adjust the observational data, the typical size of the void in LTB models is of the order of Gpc. The last parameter $\Omega_{M,\text{out}}$, as previously mentioned, was fixed to unity in order to asymptotically recover the flat FLRW model. The second profile is similar to the CGBH but has one parameter less and displays a Gaussian-like transition from inside the void to the outer region. The matter density for the Gaussian profile reads

$$\Omega_M(r) = \Omega_{M,\text{out}} + (\Omega_{M,\text{in}} - \Omega_{M,\text{out}})e^{-\left(\frac{r}{r_0}\right)^2}. \quad (21)$$

All the parameters have the same physical interpretation as before.

The third and last profile follows a similar reasoning of the previous parameterization. It is a void model that smoothly changes the matter density from an underdense environment with $\Omega_{M,\text{in}}$ to an outer denser region with matter density $\Omega_{M,\text{out}}$. The profile reads

$$\Omega_M(r) = \Omega_{M,\text{in}} + (\Omega_{M,\text{out}} - \Omega_{M,\text{in}}) \frac{\left(\frac{r}{r_0}\right)^{3+\nu} \left[1 + \nu \ln^2\left(\frac{r}{r_0}\right)\right]}{1 + \left(\frac{r}{r_0}\right)^{3+\nu} \left[1 + \nu \ln^2\left(\frac{r}{r_0}\right)\right]}, \quad (22)$$

where ν plays a similar role as Δr for the CGBH profile. A nice feature that distinguishes the above profile from the CGBH is the independence of the value of the matter density at r_0 with respect to the transition parameter. In the $C\nu$ -ln2 parameterization $\Omega_M(r_0)$ depends only on $\Omega_{M,\text{in}}$ and $\Omega_{M,\text{out}}$. Indeed, a direct calculation shows that

$$\Omega_M(r_0) = \frac{\Omega_{M,\text{in}} - \Omega_{M,\text{out}} \tanh(r_0/2\Delta r)}{1 + \tanh(r_0/2\Delta r)} \quad \text{CGBH profile} \quad (23)$$

$$\Omega_M(r_0) = \frac{1}{2}(\Omega_{M,\text{out}} + \Omega_{M,\text{in}}) \quad \text{C}\nu\text{-ln2 profile} \quad (24)$$

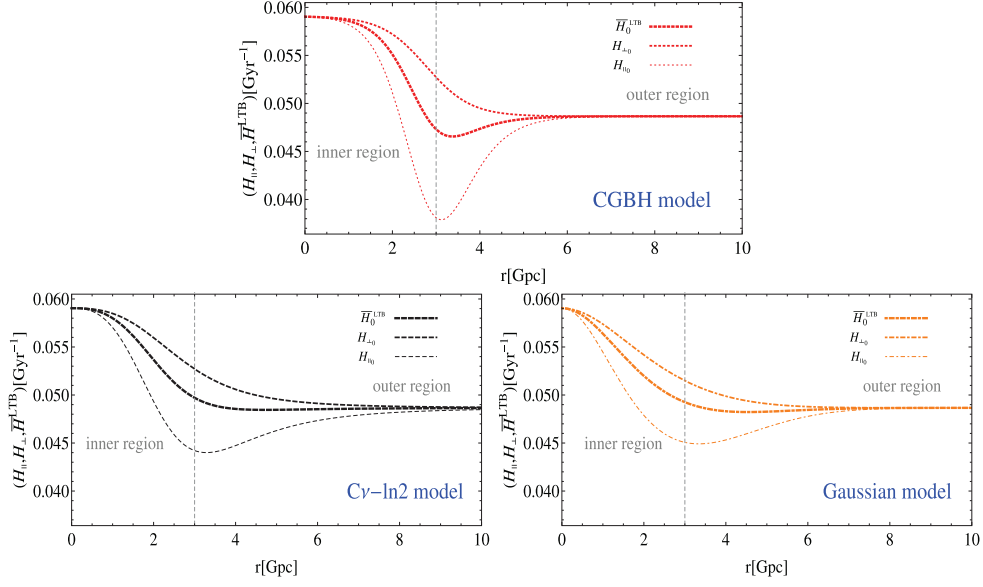


Figure 2. Plot of the three expansion rates today: transverse $H_{\perp 0}(r)$, the radial $H_{\parallel 0}(r)$ and the geometrical mean $\bar{H}_{\text{LTB}}(t_0, r)$. The parameters used to plot the three profiles was $\Omega_{M\text{out}} = 1$, $\Delta r = \nu = 0.5$, $\Omega_{M\text{in}} = 0.3$ and $r_0 = 3$.

In figure 2, we depict the transverse and radial expansion rates (2) and the geometrical mean \bar{H}^{LTB} for these three different profiles. It is worth noting that for the CGBH model the difference between the transverse and radial expansion rates is prominently larger than in the other models.

3.1. Deceleration parameter

The two expansion rates in an LTB model, viz. the transverse $H_{\perp 0}(r)$ and the radial $H_{\parallel 0}(r)$ expansion rates, can be used to define two different deceleration parameters. Thus, in analogy to the FLRW metric, we can define the transverse and radial deceleration parameters as

$$q_{\perp}(t, r) = -\frac{\ddot{X}(t, r)}{X(t, r)H_{\perp}^2(t, r)}, \quad (25)$$

$$q_{\parallel}(t, r) = -\frac{\ddot{X}'(t, r)}{X'(t, r)H_{\parallel}^2(t, r)}. \quad (26)$$

The LTB solution reduces to an FLRW metric when $X(r, t) = a(t)r$, with $a(t)$ being the scale factor. One can immediately verify that in this case both deceleration parameters defined above merge into the FLRW parameter, i.e. $q = q_{\parallel} = q_{\perp} = -\frac{\ddot{a}}{aH^2}$. Figure 3 shows both deceleration parameters as a function of radius at different times.

In all cases the expansion today is decelerated contrasting with the Λ CDM model that describes a late time accelerating universe. This is a general feature of LTB models which is considered in the literature as a powerful manner to distinguish a homogeneous and isotropic evolution from inhomogeneous models [37, 38].

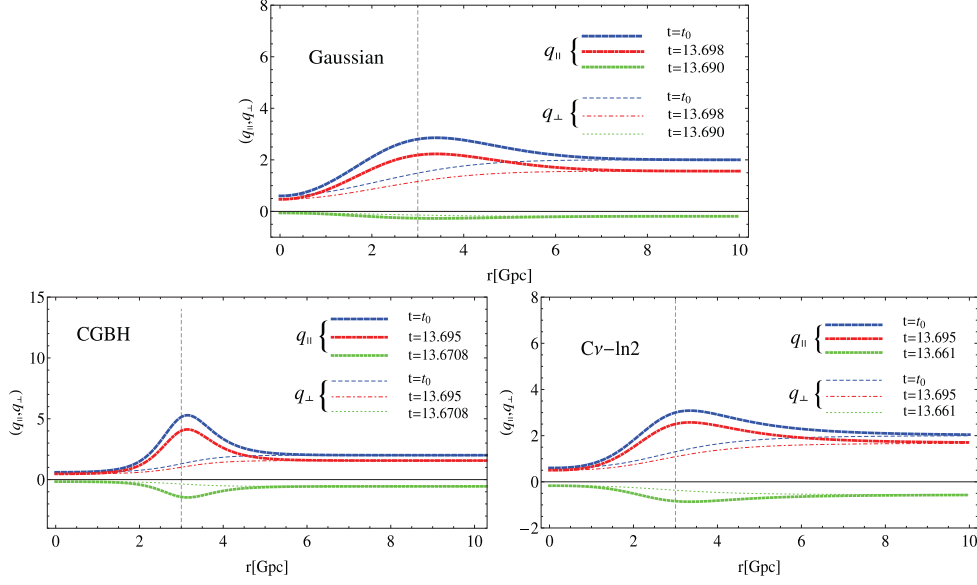


Figure 3. Plot of the radial and transverse deceleration parameters as a function of r at different times. The vertical dashed line marks the typical size of the void r_0 . Note that close to time t_0 all the curves are positive, hence, displaying deceleration universes today.

Besides the two deceleration parameters defined above, we can still combine them to form an effective deceleration parameter. In LTB spacetimes the expansion factor of a time-like congruence of static observers with $v^\mu = \delta_0^\mu$ is given by $\Theta = \nabla_\nu v^\mu = H_{\parallel} + 2H_{\perp}$. On the other hand, in an FLRW universe we can write the deceleration parameter as $q = -1 - 3\dot{\Theta}/\Theta$. Therefore, we define an effective LTB deceleration parameter simply by replacing the expansion factor for its LTB version. Using (15), the effective deceleration parameter in terms of the redshift reads

$$q^{\text{eff}}(z) = -1 + \frac{3(1+z)H_{\parallel}(z)}{[H_{\parallel}(z) + 2H_{\perp}(z)]^2} \left[\frac{d}{dz} H_{\parallel}(z) + 2 \frac{d}{dz} H_{\perp}(z) \right]. \quad (27)$$

Note that for large redshift the effective parameter approaches the FLRW behaviour. Figure 4 shows the evolution in redshift of the effective deceleration parameter for the three profiles. Additionally, we included for comparison the flat Λ CDM (with $\Omega_m = 0.3$) and the Einstein-de Sitter (EdS) models. The deceleration parameter for all inhomogeneous models changes sign twice displaying decelerating expansion for small z . This behaviour is in agreement with the transverse and parallel deceleration parameters described above.

3.2. BAO in LTB models

The standard model describes the primordial nucleosynthesis and recombination processes within a homogeneous and isotropic universe. The BAO is a characteristic length scale imprinted in the matter distribution that encodes the physics of this early phase of the universe. This small signal excess occurs at length separations of the order of 150 Mpc.

In order to deal with BAO observations in inhomogeneous models, one has to tackle different effects coming from the spatial dependence of the background dynamics. In particular, in

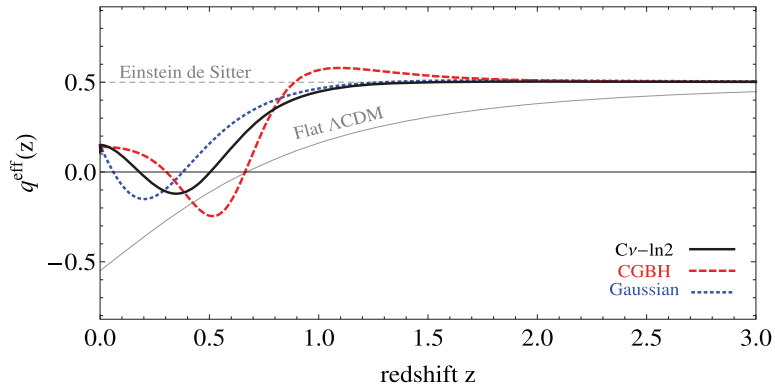


Figure 4. Effective deceleration parameter for the three models compared with the flat Λ CDM and the EdS model.

an LTB model the physical length depends not only on time but also on the radial coordinates. Furthermore, the model has two distinct expansion rates, i.e. the transverse $H_{\perp}(t, r)$ and the radial $H_{\parallel}(t, r)$ expansion rates. In an arbitrary inhomogeneous model, one has to start the BAO analysis from first principles. However, the profiles (20)–(22) together with the hypothesis of a simultaneous Big Bang time guarantee that our LTB models have the valuable property of approaching the FLRW dynamics in the far past. Therefore, we can assume that these models are indistinguishable from an FLRW universe during recombination. The crucial step is then to properly propagate the initial condition through the inhomogeneous LTB dynamics. The transverse and radial components evolve differently, hence, following [39], we should describe them separately.

The spherical symmetry of the LTB metric considerably simplifies the evolution of the transverse length. Indeed, one can choose the coordinate systems such that $\dot{\theta} = \dot{\varphi} = 0$. In addition, these conditions are stable for timelike geodesics. Therefore, an initial angular separation $d\theta$ between neighbor geodesics is preserved along the trajectory. Thus, the angular physical length at emission is given by $L_{\perp}(t_e, r) = \int \sqrt{g_{\theta\theta}} d\theta = X(t_e, r) d\theta$. The radial physical length is obtained in a similar manner. A material particle initially at rest will continue at the same radial position and this evolution is again stable for timelike geodesics. For an initial radial separation dr , the radial physical length at emission is $L_{\parallel}(t_e, r) = \int \sqrt{g_{rr}} dr \approx X'(t_e, r) dr / \sqrt{1 + 2E(r)}$. These lengths can be related to the observed physical lengths, respectively, as

$$L_{\perp}(t, r) = \frac{X(t, r)}{X(t_e, r)} L_{\perp}(t_e, r), \quad (28)$$

$$L_{\parallel}(t, r) = \frac{X'(t, r)}{X'(t_e, r)} L_{\parallel}(t_e, r). \quad (29)$$

The above relations express the background evolution of the physical length in the LTB model. The first-order corrections are not so straightforward as in the homogeneous and isotropic case. In an FLRW universe, the evolution of sub-horizon first-order perturbations is exclusively time dependent, hence, spatial dependence on BAO scale comes only from non-linear corrections. Nowadays cosmological observations precision is accurate enough to urge for an adequate control of these effects. As argued in [40–42] these effects can produce a shift in the acoustic scale, which in turn might generate systematics compared to expected

statistical errors in the next generation of surveys. Notwithstanding, for the present analysis we shall keep only up to first-order perturbations.

The evolution of linear perturbations in inhomogeneous models is more complicated than in FLRW. One of the key issues is the mixing of first-order perturbation modes. As is well known [33, 43], the decoupling of linear order perturbations is a direct consequence of the symmetries of the background FLRW metric. In an LTB universe a coupling is expected between the scalar, vector and tensor modes. The crucial coupling in an LTB universe is between the scalar and tensor modes. Indeed, due to the spherical symmetry of the background LTB metric, it can be shown that vector modes can be disregarded compared to the other components. Furthermore, the mode-coupling depends on the specific matter profile of the model. Fortunately, for the CGBH profile these nonlinear effects are subdominant [39, 44] and one can approximately consider the BAO scale to be constant in coordinate space. The validity for the Gaussian and $C\nu$ -ln2 profiles follows from their lower difference between the radial and transverse expansion rates (see figure 2).

The LTB models considered here approach the dust FLRW behaviour either for large spatial distances ($r = r_\infty \gg r_0$) or far in the past ($t = t(z_\infty)$ with $z_\infty \gtrsim 1000$). Therefore, we can assume that early times baryonic dynamics in our model is indistinguishable from the FLRW case. This feature guarantees the use of the spatial independent Big Bang BAO scale as an initial condition for our models. Additionally, in the far past, the approximate homogeneity and isotropy of the universe allows us to assume the BAO scale to be spatial coordinate independent at constant time hypersurfaces

$$L^{\text{BAO}}(t_e, r(z)) \approx L^{\text{BAO}}(t_e, r_\infty). \quad (30)$$

The asymptotic BAO scale can be computed within a Λ CDM scenario for which we use the fitting formulae for an adiabatic cold dark matter developed in [45]. The asymptotic BAO scale depends on the sound horizon l_s at the drag epoch which can be approximated by

$$l_s(z_{\text{drag}}) = \frac{44.5 \ln(9.83/\Omega_M^{\text{eff}} h_{\text{eff}}^2)}{\sqrt{1 + 10(\Omega_b^{\text{eff}} h_{\text{eff}}^2)^{3/4}}} \text{Mpc}, \quad (31)$$

where Ω_M^{eff} , Ω_b^{eff} and h_{eff} are, respectively, the effective total density, effective baryon density and the effective normalised Hubble factor. In a conventional Λ CDM model we would have instead the total matter parameter Ω_0 , the baryonic parameter Ω_b and the normalised Hubble factor $h = H_0/(100 \text{ Km} \cdot \text{Mpc}^{-1} \cdot \text{s}^{-1})$. However, since in the asymptotic regime our model is only approximately homogeneous and isotropic we need to evolve backwards in time the LTB dynamics up to the time of emission and use the effective values in the above fitting formulae.

The emission time has to be far enough in the past to reach the asymptotic FLRW behaviour. Due to computational economy we select the emission time as $z_e = 100$ when the LTB inhomogeneities⁷ are still of the order of 1%. At this stage we can assume $\Omega_M^{\text{eff}} = \Omega_{M\text{out}}$ and $\Omega_b^{\text{eff}} = f_b \Omega_{M\text{out}}$ where f_b is the fraction of baryon to total matter. The normalised Hubble factor reads $h_{\text{eff}} = H_0^{\text{eff}}/(100 \text{ Km} \cdot \text{Mpc}^{-1} \cdot \text{s}^{-1})$ where the effective Hubble parameter is given by

⁷The inhomogeneities can be characterized through the density contrast $\delta\rho_m(t, r) = \rho_m(t, r)/\rho_m(t_\infty, r)$, hence, the statement that LTB inhomogeneities are small means that $\delta\rho(t, r) \lesssim 1\%$.

$$H_0^{\text{eff}} = \frac{[H_{\parallel}(z_e)H_{\perp}^2(z_e)]^{1/3}}{\sqrt{\Omega_M^{\text{eff}}(1+z_e)^3 + (1-\Omega_M^{\text{eff}})(1+z_e)^2}}. \quad (32)$$

The single difference in the above procedure from [39] is the use of the geometrical mean Hubble parameter (3), instead of the arithmetic mean Hubble parameter (7). This modification has the advantage of the geometrical mean converge faster to the FLRW regime than the arithmetic mean.

The sound horizon gives the comoving BAO scale which in a flat FLRW universe equals the physical BAO scale today⁸. Recalling that the asymptotic spatial limit of the LTB model at any time is an FLRW universe, we have $L^{\text{BAO}}(t_0, r_{\infty}) = l_s(z_{\text{drag}})$. In order to relate the sound horizon (31) with the radial and transverse physical scales using (28)–(30) one performs a cross-multiplication to obtain

$$L_{\parallel}^{\text{BAO}}(z) = \frac{X'(t(z), r(z))}{X'(t_e, r(z))} \frac{X'(t_e, r_{\infty})}{X'(t_0, r_{\infty})} l_s(z_{\text{drag}}), \quad (33)$$

$$L_{\perp}^{\text{BAO}}(z) = \frac{X(t(z), r(z))}{X(t_e, r(z))} \frac{X(t_e, r_{\infty})}{X(t_0, r_{\infty})} l_s(z_{\text{drag}}). \quad (34)$$

There is one last step to connect the above relations to the observational data. The sensitivity of current surveys provides only a combined distance scale ratio from the spherically averaged power spectrum [46, 47]. In an FLRW universe, the physical observable associated with the BAO scale is the ratio

$$\theta_{\text{FLRW}} = \frac{l_s(z_{\text{drag}})}{D_V^{\text{FLRW}}(z)}, \quad (35)$$

where $D_V^{\text{FLRW}}(z)$ encodes the dilation scale as the cube root of the product of the radial dilation with the square of the transverse dilation [6, 48]. The radial dilation is given by $D_z^{\text{FLRW}}(z) = z/H^{\text{FLRW}}(z)$, whereas the angular or transverse dilation is simply the comoving angular diameter distance that can be written in term of the diameter distance as $(1+z)D_A^{\text{FLRW}}$. Thus, we write

$$D_V^{\text{FLRW}}(z) = \left[((1+z)D_A^{\text{FLRW}})^2 \frac{z}{H^{\text{FLRW}}(z)} \right]^{1/3}. \quad (36)$$

Even though (35) gives a BAO observable, actual measurements usually refer to the model-independent quantities $(\Delta\theta^2\Delta z)$ where $\Delta\theta$ is the angular in the sky and Δz is the redshift interval corresponding to the comoving sound horizon. In an FLRW universe we have $D_A = l_s/(1+z_{\text{BAO}})\Delta\theta$ and $l_s = \Delta z/H(z_{\text{BAO}})$ hence we find

$$(\Delta\theta^2\Delta z)^{1/3} = z^{1/3} \frac{l_s}{D_V(z)} \quad \text{for FLRW.} \quad (37)$$

In accordance with [39, 49], we shall define in the LTB model a characteristic BAO length $d_z(z)$ as the LTB analogue of the above relation. Thus, we define the length

$$d_z(z) = \left(\frac{\Delta\theta^2\Delta z}{z} \right)^{1/3} \quad \text{for LTB.} \quad (38)$$

⁸The identification of the comoving sound horizon with the physical BAO scale today is valid if we assume the normalization of the scale factor $a(t_0) = 1$.

The angular scale is again related to the angular diameter distance with the difference that we must use the transverse BAO length

$$\Delta\theta_{\text{BAO}} = \frac{L_{\perp}^{\text{BAO}}(z)}{d_A^{\text{LTB}}(z)}. \quad (39)$$

In a similar manner, from (16) and the metric (1), the redshift separation reads

$$\Delta z_{\text{BAO}} = (1+z)H_{\parallel}(z)L_{\parallel}^{\text{BAO}}(z). \quad (40)$$

Thus, combining the above equations with (33) and (34) we obtain

$$d_z^{\text{LTB}} = \left[\frac{1+z}{z} \frac{H_{\parallel}(z)}{d_A^{\text{LTB}}(z)^2} \right]^{1/3} \xi(z) l_s(z_{\text{drag}}), \quad (41)$$

where the redshift dependent function $\xi(z)$ reads

$$\xi(z) = \left(\frac{X'(t(z), r(z))}{X'(t_e, r(z))} \frac{X'(t_e, r_{\infty})}{X'(t_0, r_{\infty})} \right)^{1/3} \left(\frac{X(t(z), r(z))}{X(t_e, r(z))} \frac{X(t_e, r_{\infty})}{X(t_0, r_{\infty})} \right)^{2/3}. \quad (42)$$

4. Observational data

4.1. Type Ia supernovae

In this paper we use the joint light-curve analysis sample [26] which is known in the literature as the JLA sample. This extended sample of 740 spectroscopically confirmed type Ia supernovae with high quality light curves consist of several low-redshift samples ($z < 0.1$), the third year sample from the Sloan Digital Sky Survey (SDSS-II, $0.05 < z < 0.4$), the third year superNova legacy survey (SNLS, $0.2 < z < 1$) and the Hubble space telescope sample (HST, $z > 1$). The observational distance modulus is modeled, in the context of the light curve fitter spectral adaptive light curve template (SALT2) [50], by

$$\mu_i^{\text{SNIa}} = m_{B,i}^* + \alpha X_{1,i} - \beta C_i - M_B \quad (43)$$

where α , β and M_B are nuisance parameters in the distance estimate which are fitted simultaneously with the cosmological parameters. The absolute B -band magnitude is related to the host stellar mass (M_{stellar}) by a simple step function

$$M_B = \begin{cases} M_B^1 & \text{if } M_{\text{stellar}} < 10^{10} M_{\odot} \\ M_B^1 + \Delta_M & \text{otherwise} \end{cases} \quad (44)$$

The light-curve parameters (m_B^* , X_1 , C) result from the fitting of a model of SNe Ia spectral sequence to the photometric data. We can build the χ^2 function as

$$\chi^2(\boldsymbol{\theta}, \boldsymbol{\delta}, M_B) = \sum_{i=1}^{740} \frac{[\mu_i^{\text{SNIa}}(\boldsymbol{\delta}, M_B) - \mu_{\text{th}}^{\text{LTB}}(z_i; \boldsymbol{\theta})]^2}{\sigma_i^2 + \sigma_{\text{int}}^2} \quad (45)$$

where the supernovae parameters are denoted by $\boldsymbol{\delta} := (\alpha, \beta)$ and the cosmological parameters by $\boldsymbol{\theta} := (\Omega_{M\text{in}}, \Delta r, \nu, r_0)$. The propagated error from the covariance matrix of the light-curve fitting is

Table 1. BAO data summarized.

Sample	z	$d_z \pm \sigma_{d_z}$
6dFGS	0.106	0.336 ± 0.015
SDSS	0.35	0.1126 ± 0.0022
SDSS	0.57	0.0732 ± 0.0012
WiggleZ	0.44	0.0916 ± 0.0071
WiggleZ	0.6	0.0726 ± 0.0034
WiggleZ	0.73	0.0592 ± 0.0032
Sample	z	$\Delta\theta \pm \sigma_\theta$
Carnero <i>et al</i>	0.55	$3.90^\circ \pm 0.38^\circ$

$$\sigma_i^2 = \sigma_{m_B^*,i}^2 + \alpha^2 \sigma_{X_i,i}^2 + \beta^2 \sigma_{C,i}^2 + 2\alpha\sigma_{m_B^*X_i,i} - 2\beta\sigma_{m_B^*C,i} - 2\alpha\beta\sigma_{X_iC,i} + \sigma_{\mu z,i}^2, \quad (46)$$

where $\sigma_{\mu z,i}^2$ represents the contribution to the distance modulus coming from redshift uncertainties and peculiar velocities. Following [51, 52] we shall simulate these effects by the distance-redshift relation for an empty universe, hence

$$\sigma_{\mu z,i} = \sigma_{z,i} \left(\frac{5}{\log 10} \right) \frac{1 + z_i}{z_i(1 + z_i/2)}. \quad (47)$$

In the above expression $\sigma_{z,i}^2 = \sigma_{\text{spec},i}^2 + \sigma_{\text{pec}}^2$ with $\sigma_{\text{spec},i}$ representing the redshift measurement error and $\sigma_{\text{pec}} = 0.0012$ is the uncertainty due to peculiar velocity. Finally, a floating term σ_{int} is also included in (45) to account for both intrinsic variations in the supernova luminosity and systematic effects.

Originally, the term σ_{int} was not considered as a free parameter to be optimised in the χ^2 approach but should rather be determined by an iterative procedure. We start with a guess value for σ_{int} (usually around 0.15) and perform the minimization procedure to obtain the best-fit values for the supernova and cosmological parameters. Then, with these best-fit values, we fine-tune σ_{int} such that the reduced χ^2 goes to unity. The procedure is repeated with this new value of σ_{int} as input. The iteration ends when the value of σ_{int} converges.

The authors of [51] have exposed the limits of validity of the usual uncorrected χ^2 approach. This happens when the covariance depends on the free parameters of the underlying model. In this case, one should use a parameter fitting based on the Likelihood function

$$\mathcal{L}(\boldsymbol{\theta}, \boldsymbol{\delta}, M_B, \sigma_{\text{int}}) := \chi^2(\boldsymbol{\theta}, \boldsymbol{\delta}, M_B, \sigma_{\text{int}}) + \sum_i^N \ln(\sigma_i^2(\boldsymbol{\delta}) + \sigma_{\text{int}}^2), \quad (48)$$

where now σ_{int} is also considered as a free parameter. In this paper we shall follow both methods and compare their results in section 5.

4.2. The BAO sample

The characteristic BAO scale detected in the correlation function of different matter distribution gives a powerful standard ruler to probe the angular diameter distance-redshift relation and the Hubble parameter. The BAO scale has been measured at different redshift values, namely at $z = 0.106$ by the 6dFGS [53], $z = 0.35$ and 0.57 by the SDSS [54, 55], $z = 0.44$, 0.6 and 0.73 by the WiggleZ collaboration [56]. There is also an additional point presented by Carnero *et al* [57] at $z = 0.55$ indicating the angular correlation. All data are summarized in the table 1.

Then, the Likelihood approach is thus given by

$$\chi_{\text{BAO}}^2 = \sum_{ij} [d_{z,i} - d_z^{\text{LTB}}(z_i; \gamma)] C_{ij}^{-1} [d_{z,j} - d_z^{\text{LTB}}(z_j; \gamma)] + \frac{[\Delta\theta - \Delta\theta_{\text{BAO}}(0.55)]^2}{\sigma_\theta^2} \quad (49)$$

where $\gamma := (\Omega_{M,\text{in}}, \Delta r, \nu, r_0, f_b)$ and C_{ij}^{-1} is the inverse covariance matrix expressed in terms of the d_z :

$$C_{ij}^{-1} = \begin{pmatrix} 4444 & 0. & 0. & 0. & 0. & 0. \\ 0. & 206\,612 & 0 & 0. & 0. & 0. \\ 0. & 0 & 694\,444 & 0. & 0. & 0. \\ 0. & 0. & 0. & 23\,857 & -22\,747 & 10\,586 \\ 0. & 0. & 0. & -22\,747 & 128\,729 & -59\,907 \\ 0. & 0. & 0. & 10\,586 & -59\,907 & 125\,536 \end{pmatrix}. \quad (50)$$

5. Results

In this section we describe the result of the best fit parameters of the LTB model for the three profiles. Both the CGBH and $C\nu\text{-ln}2$ profiles have three parameters to specify their matter distribution plus an extra parameter f_b in order to include the BAO analysis. In contrast, the Gaussian profile has only two parameters plus the f_b . Apart from this, there is also the supernovae parameters (α , β , M_B^1 and Δ_M) which, naturally, are the same for all cases. The numerical results are summarized in tables 2–4. For comparison, the table 5 show the results of a corresponding analysis for the flat ΛCDM model setting $H_0 = 71 \text{ Km Mpc}^{-1} \text{ s}^{-1}$.

Table 2 shows the best fit parameters for the CGBH model using the χ^2 and Likelihood approaches. We display the best fit values separately for the JLA, the BAO and the JLA + BAO combined analysis. Tables 3 and 4 show, respectively, the same information for the Gaussian and $C\nu\text{-ln}2$ profiles. Note that the supernovae parameters (α , β , M_B^1 and Δ_M) have similar results for the three cases. This is consistent with the idea that these parameters are not very sensitive to cosmological evolution. In contrast, the cosmological parameters ($\Omega_{M,\text{in}}$, Δr , ν and r_0) do show some appreciable differences. In particular, the $C\nu\text{-ln}2$ model requires the highest matter density within the void $\Omega_{M,\text{in}}$ relative to the CGBH and Gaussian models. This feature is robust in the sense that it appears in both χ^2 and Likelihood approaches.

The contour levels for each profile using only SNIa, i.e. only the JLA sample, are depicted in figures 5–7. In these figures, the dashed contours indicate the 1σ , 2σ and 3σ confidence regions for the χ^2 approach, while the solid lines show the contours for the Likelihood approach. Figure 5 displays the Gaussian profile while the CGBH and $C\nu\text{-ln}2$ profiles are shown, respectively, in figures 6 and 7. Note that the contour levels for the χ^2 and Likelihood approaches are similar in shape and area. However, there is an interesting difference from the results of [51]. Here there is a significant bias in the best fit values and the Likelihood contours are slightly bigger than the χ^2 .

Figures 8 and 9 display the 1D probability distributions function (PDF) of the σ_{int} parameter for all models. Figure 8 considers only the JLA sample while figure 9 depicts the combined analysis of JLA + BAO. The dashed straight line in each panel indicates the value obtained from the χ^2 approach. Note that in all cases the χ^2 values are excluded with respect to the Likelihood approach. This can also be seen through the contour levels. The two approaches give disjoint results at 1σ in the planes (β, r_0) , (β, α) , $(\Delta r, \beta)$, (ν, β) and $(\Omega_{M,\text{in}}, \beta)$. Thus, our analysis exhibits a concrete example of the issues and criticisms related to the χ^2 approach discussed in [51].

Table 2. Best fit parameters for the CGBH model in the χ^2 and Likelihood approaches.

CGBH	Ω_{Min}	r_0	Δr	$100 f_b$	α	β	M_B^1	Δ_M	$\chi_{min}^2/\text{d.o.f.}$	σ_{int}
χ_{JLA}^2	$0.09_{-0.02}^{+0.03}$	$3.88_{-2.12}^{+2.47}$	$3.89_{-2.44}^{+2.12}$	$0.12_{-0.02}^{+0.02}$	$2.66_{-0.19}^{+0.19}$	$-19.22_{-0.05}^{+0.05}$	$-0.04_{-0.03}^{+0.03}$	713.61/733	0.02
\mathcal{L}_{JLA}	$0.11_{-0.03}^{+0.03}$	$4.15_{-2.42}^{+2.97}$	$3.79_{-2.85}^{+2.34}$	$0.11_{-0.02}^{+0.02}$	$2.26_{-0.20}^{+0.20}$	$-19.25_{-0.05}^{+0.05}$	$-0.03_{-0.35}^{+0.35}$	$0.06_{-0.03}^{+0.03}$
χ_{BAO}^2	$0.38_{-0.06}^{+0.08}$	$3.31_{-0.46}^{+1.22}$	$0.51_{-0.17}$	$5.62_{-3.92}^{+5.53}$	1.03/3
$\chi_{JLA+BAO}^2$	$0.12_{-0.02}^{+0.02}$	$3.16_{-0.17}^{+0.17}$	$0.73_{-0.15}^{+0.97}$	$15.30_{-0.70}^{+8.59}$	761.07/743	0.03
$\mathcal{L}_{JLA+BAO}$	$0.12_{-0.02}^{+0.02}$	$3.72_{-0.29}^{+0.31}$	$1.68_{-0.32}^{+0.60}$	$16.81_{-0.32}^{+7.69}$	$0.07_{-0.02}^{+0.02}$

Table 3. Best fit parameters for the Gaussian model in the χ^2 and Likelihood approaches.

Gaussian	Ω_{Min}	r_0	$100 f_b$	α	β	M_B^1	Δ_M	$\chi_{min}^2/\text{d.o.f.}$	σ_{int}
χ_{JLA}^2	$0.16_{-0.02}^{+0.02}$	$4.28_{-0.66}^{+0.99}$	$0.12_{-0.02}^{+0.02}$	$2.65_{-0.18}^{+0.18}$	$-19.27_{-0.04}^{+0.04}$	$-0.04_{-0.03}^{+0.03}$	714.56/734	0.03
\mathcal{L}_{JLA}	$0.17_{-0.02}^{+0.02}$	$4.27_{-0.75}^{+1.23}$	$0.11_{-0.02}^{+0.02}$	$2.25_{-0.19}^{+0.19}$	$-19.30_{-0.05}^{+0.04}$	$-0.03_{-0.03}^{+0.03}$	$0.07_{-0.03}^{+0.02}$
χ_{BAO}^2	$0.26_{-0.06}$	$7.39_{-1.48}$	$18.9_{-13.29}$	1.09/4
$\chi_{JLA+BAO}^2$	$0.17_{-0.01}^{+0.01}$	$5.08_{-0.27}^{+0.32}$	$16.31_{-1.98}^{+2.23}$	741.52/744	0.02
$\mathcal{L}_{JLA+BAO}$	$0.19_{-0.02}^{+0.02}$	$5.04_{-0.35}^{+0.40}$	$14.49_{-2.20}^{+2.33}$	$0.07_{-0.02}^{+0.02}$

Table 4. Best fit parameters for the $C\nu$ -ln2 model in the χ^2 and Likelihood approaches.

$C\nu$ ln-2	Ω_{Min}	r_0	ν	$100 f_b$	α	β	M_B^1	Δ_M	χ_{min}^2 /d.o.f.	σ_{int}
χ_{JLA}^2	$0.18_{-0.02}^{+0.02}$	$3.12_{-0.46}^{+0.61}$	$0.04^{+1.66}$	$0.12_{-0.16}^{+0.16}$	$2.63_{-0.19}^{+0.19}$	$-19.29_{-0.04}^{+0.04}$	$-0.05_{-0.03}^{+0.03}$	713.98/733	0.03
\mathcal{L}_{JLA}	$0.21_{-0.03}^{+0.02}$	$3.02_{-0.50}^{+0.69}$	$0.08^{+2.28}$	$0.11_{-0.02}^{+0.02}$	$2.23_{-0.20}^{+0.20}$	$-19.33_{-0.05}^{+0.05}$	$-0.03_{-0.03}^{+0.03}$	$0.07_{-0.03}^{+0.03}$
χ_{BAO}^2	$0.26_{-0.12}$	$5.23_{-1.65}$	$0.58^{+4.95}$	$19.54^{+2.53}$	1.21/3
$\chi_{JLA+BAO}^2$	$0.21_{-0.02}^{+0.02}$	$4.40_{-0.36}^{+0.40}$	$0.34^{+1.45}$	$20.97_{-3.30}^{+3.09}$	742.59/743	0.14
$\mathcal{L}_{JLA+BAO}$	$0.22_{-0.02}^{+0.02}$	$3.54_{-0.24}^{+0.29}$	$0.03^{+1.46}$	$11.65_{-2.13}^{+2.42}$	$0.07_{-0.02}^{+0.02}$

Table 5. Best fit parameters for the Λ CDM model in the χ^2 and Likelihood approaches.

Λ CDM	Ω_M	$100f_b$	α	β	M_B^1	Δ_M	$\chi_{\min}^2/\text{d.o.f.}$	σ_{int}
χ_{JLA}^2	$0.312^{+0.030}_{-0.029}$...	$0.123^{+0.014}_{-0.014}$	$2.665^{+0.158}_{-0.158}$	$-19.022^{+0.023}_{-0.023}$	$-0.043^{+0.021}_{-0.022}$	715.793/735	0.019
\mathcal{L}_{JLA}	$0.329^{+0.034}_{-0.032}$...	$0.107^{+0.015}_{-0.015}$	$2.265^{+0.172}_{-0.170}$	$-19.032^{+0.029}_{-0.026}$	$-0.028^{+0.024}_{-0.024}$...	$0.064^{+0.022}_{-0.027}$
χ_{BAO}^2	$0.255^{-0.195}$	$21.325_{-14.08}$	1.997/5
$\chi_{\text{JLA+BAO}}^2$	$0.312^{+0.026}_{-0.025}$	$14.712^{+3.867}_{-3.193}$	718.035/745	0.019
$\mathcal{L}_{\text{JLA+BAO}}$	$0.328^{+0.019}_{-0.019}$	$13.301^{+2.479}_{-2.181}$	$0.054^{+0.018}_{-0.019}$

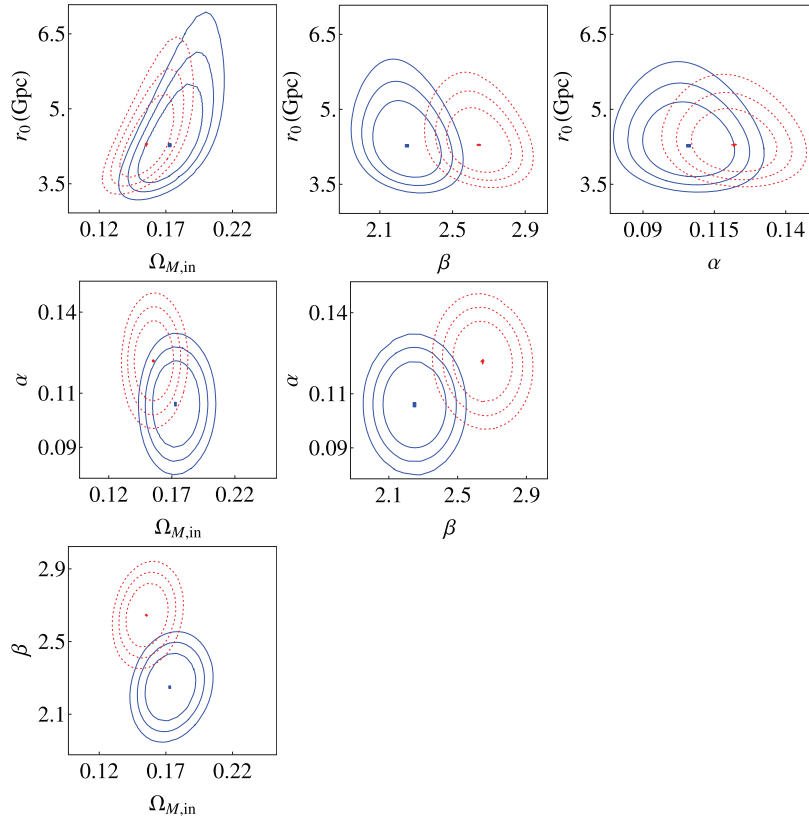


Figure 5. Contour Level best fit parameters in the χ^2 (dashed red lines) and likelihood (solid blue lines) approaches with the JLA sample only for the Gaussian model.

In section 3.2 we introduced the parameter f_b and described how one can use standard rulers (BAO) within LTB scenarios. Independently of the statistical approach used (χ^2 or Likelihood), there appears a tension between BAO and SNIa best fit results (see the planes $(\Omega_{M,in}, r_0)$ and $(\Omega_{M,in}, \Delta r)$ in figure 10 and the planes $(\Omega_{M,in}, \nu)$ and (ν, r_0) in figure 12). It has been argued in the literature (see [39]) that this discrepancy comes from the evolution of a non-zero shear in LTB models. Indeed, the spatial dependence and the difference in the evolution of the two LTB expansion rates (H_{\parallel} and H_{\perp}) work differently in fitting BAO and SNIa data. In particular, the low value of $\Omega_{M,in}$ needed to fit the SNIa data increases the expansion rate that ends up over-stretching the BAO scale near the center. In this sense, the tension observed in our analysis has a pure geometrical origin associated with the LTB dynamics. Figures 10–12 show that using only BAO to fit the parameters disagrees with the best fit of using only SNIa at least at 3σ of confidence level.

In the case of the CGBH profile model, figure 10 shows that the BAO data favours a denser void (higher matter density) as compared to the SNIa data. For the Gaussian model, figure 11 indicates that BAO favours not only higher values of matter density inside the void but also bigger voids, i.e. higher values of parameter r_0 . In the case of the $C\nu$ -ln2, there is still the same tension between BAO and SNIa best fit values yet to a smaller extent as compared to the CGBH model.

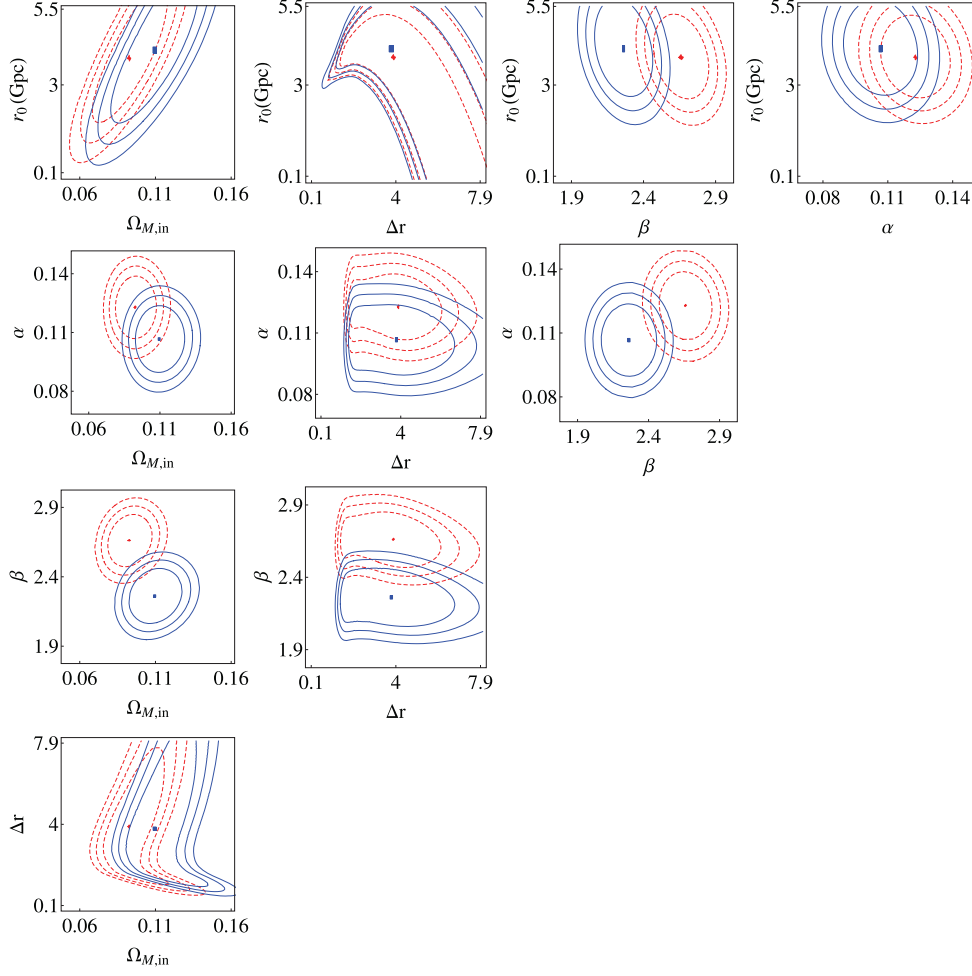


Figure 6. Contour Level best fit parameters for χ^2 (dashed red lines) and Likelihood (solid blue lines) approaches with the JLA sample only for the CGBH model.

There are several ways of performing model comparison. For instance, the (corrected) Akaike information criterion⁹ (AIC) [58] proposes to compare different models through a quantity defined as

$$AIC = \mathcal{L}_{\min} + N \ln(2\pi) + 2k + \frac{2k(k-1)}{N-k-1}, \quad (51)$$

where k is the number of free parameters and N is the number of data points. Another possibility is the Bayesian information criterion (BIC) [59] which uses the quantity

$$BIC = \mathcal{L}_{\min} + N \ln(2\pi) + k \ln N. \quad (52)$$

⁹ We have reintroduced the term $N \ln(2\pi)$, in AIC and BIC, in order to obtain the $-2 \ln \hat{\mathcal{L}}$ value, where $\hat{\mathcal{L}}$ is the maximum Likelihood function.

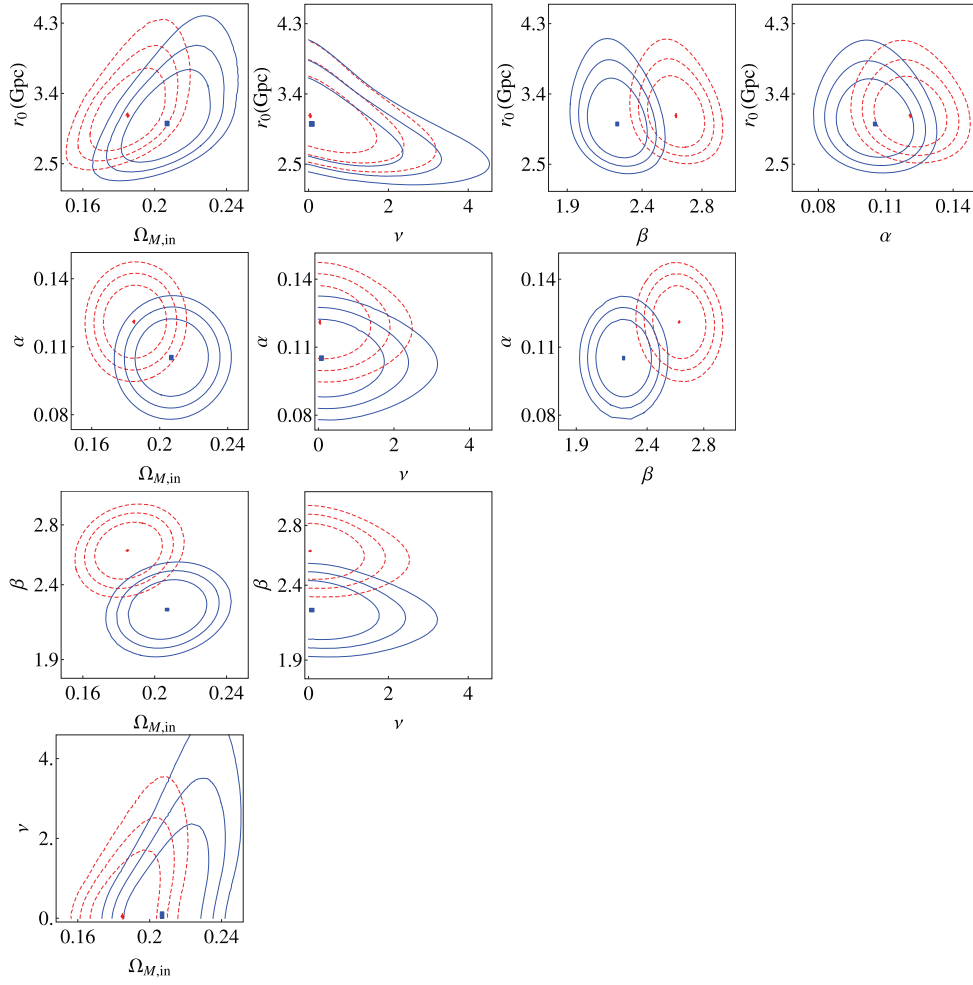


Figure 7. Contour Level best fit parameters in the χ^2 (dashed red lines) and \mathcal{L} (solid blue lines) approaches with the JLA sample only for the $C\nu$ -ln2 model.

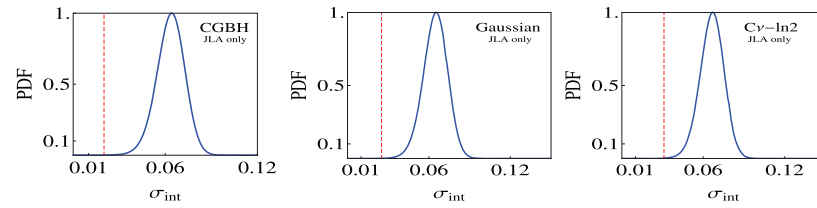


Figure 8. PDF for σ_{int} in the Likelihood approach for the CGBH (left panel), Gaussian (middle panel) and $C\nu$ -ln2 (right panel) models with the JLA only. The red dashed line indicates the values obtained in the χ^2 approach.

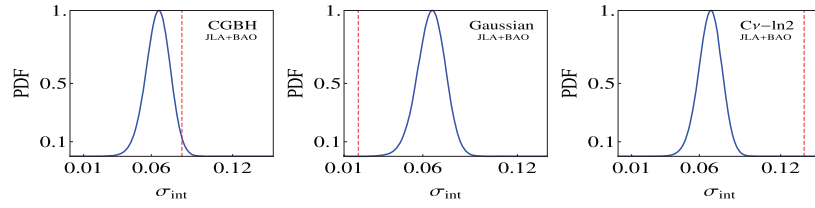


Figure 9. PDF for σ_{int} in the Likelihood approach for the CGBH (left panel), Gaussian (middle panel) and $C\nu\text{-ln}2$ (right panel) models with the combined JLA + BAO. The red dashed line indicate the values obtained in the χ^2 approach.

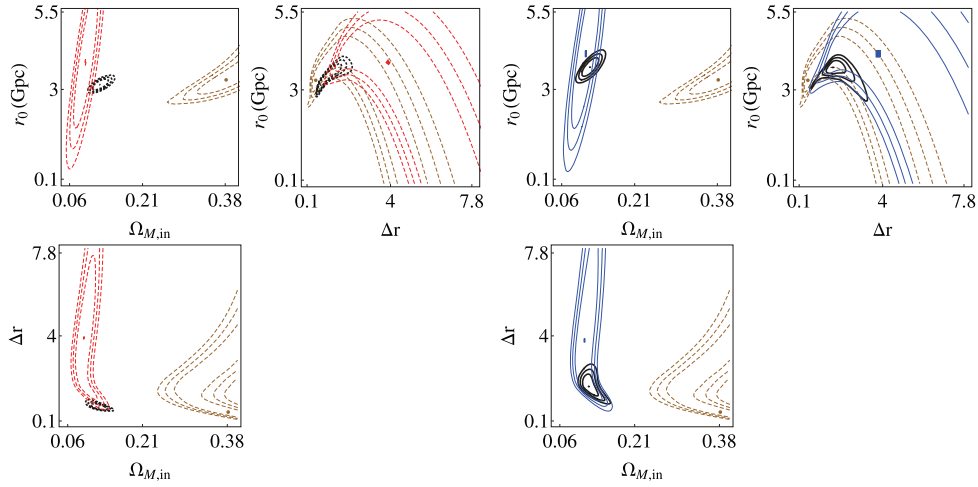


Figure 10. 1σ , 2σ and 3σ contour level best fit parameters for the CGBH model in the χ^2 approach (three left panels), with the JLA only (dashed red lines) and the combined JLA + BAO (dotted black lines), and in the Likelihood approach (three right panels), with the JLA only (solid blue lines) and the combined JLA + BAO (solid black lines). The dashed brown lines are the contours for the BAO only.

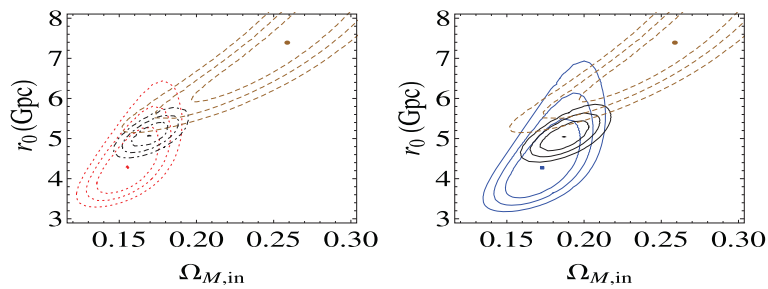


Figure 11. 1σ , 2σ and 3σ contour level best fit parameters for the Gaussian model in the χ^2 approach (left panel), with the JLA only (dashed red line) and the combined JLA + BAO (dotted black lines), and in the Likelihood approach (right panel), with the JLA only (solid blue lines) and the combined JLA + BAO (solid black lines). The dashed brown lines are the contours for the BAO only.

Table 6. Comparison of the information criterion for the best-fit parameterization of the three void models and the Λ CDM model using JLA and JLA + BAO data. The columns three and four show the difference with respect to Λ CDM model which has the lower values (*mutatis mutandis* for columns seven and eight).

Model	JLA				JLA + BAO			
	AIC	BIC	Δ AIC	Δ BIC	AIC	BIC	Δ AIC	Δ BIC
CGBH	-621.1	-584.4	2.6	11.7	-602.3	-579.3	63.7	72.9
Gaussian	-618.7	-586.6	5	9.5	-622.5	-604.1	43.5	48.1
$C\nu$ -ln2	-610.4	-573.7	13.3	22.4	-607.4	-584.4	58.6	67.8
Λ CDM	-623.7	-596.1	0	0	-666.0	-652.2	0	0

Table 7. Bayes factor for JLA and JLA + BAO, considering the Λ CDM, Gaussian, CGBH and $C\nu$ -ln2, respectively, as models 1, 2, 3 and 4.

	JLA	JLA + BAO
$2 \ln B_{12}$	9.5	48.2
$2 \ln B_{13}$	11.7	72.9
$2 \ln B_{14}$	22.4	67.8

A model is viewed as favored by the data when a lower AIC or BIC value is obtained. Note that their difference comes from the last two terms in AIC and the last one in BIC. Thus, for a large amount of data points ($N \gg 1$) BIC is a little more sensitive to an increment of parameter than AIC. Indeed, by an increment $k \rightarrow k + \delta_k$, AIC changes by an amount $2\delta_k [1 + (\delta_k + 2k - 1)/(N - \delta_k - k - 1)] + \mathcal{O}(N^{-2})$ while BIC is proportional to $\delta_k \ln N$.

Table 6 summarises the results of each profile and the Λ CDM model for SNIa and SNIa + BAO using the AIC and BIC information criterions. In both criterions the Λ CDM is favored with respect to the LTB models. Note that for the combined analysis SNIa + BAO, the Λ CDM is notoriously more favored. In order to obtain the Bayes factor B_{ij} , we can use a rough approximation [60] that is worthy as $N \rightarrow \infty$. In this limit it can be shown that

$$\frac{BIC[i] - BIC[j] + 2 \ln B_{ij}}{2 \ln B_{ij}} \rightarrow 0, \quad (53)$$

where $BIC[j]$ denotes BIC for model j . This relation is known as the Schwarz criterion and does not give the precise value of B_{ij} but it is easier to manage and does not require evaluation of prior densities through the use of the Maximum Likelihood Estimator to the parameters on each model. Of course, the relative error of this approximation is higher (of order $\mathcal{O}(1)$) and is not getting the correct value of the Bayes factor. But, keeping in mind the rough interpretation of the Bayes factor on the logarithmic scale suggested in section 3.2 of [60], the relation (53) shows that in large samples it should provide a reasonable indication of the evidence. Our results are summarized in Table 7, where we denote, respectively, the Λ CDM, Gaussian, CGBH and $C\nu$ -ln2 cases as models 1, 2, 3 and 4. It is worth noting that for the analysis using only SNIa data the evidence against the Gaussian model is strong ($6 \leq 2 \ln B_{ij} \leq 10$) in contrast with both CGBH and $C\nu$ -ln2 models which indicate very strong evidence ($2 \ln B_{ij} > 10$) to the Λ CDM model. For the JLA + BAO combined analysis the evidence of the Λ CDM is very strong against the three LTB models.

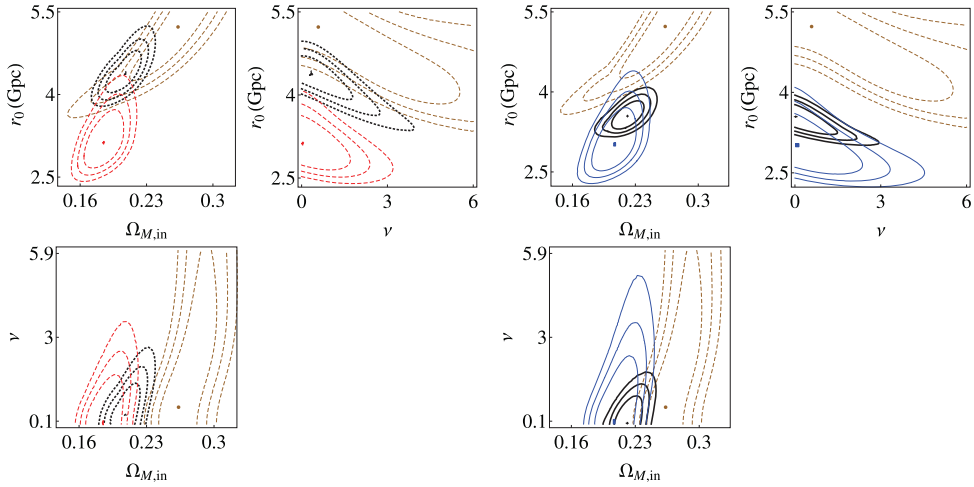


Figure 12. 1σ , 2σ and 3σ contour level best fit parameters for the $C\nu$ -ln2 model in the χ^2 approach (three left panels), with the JLA only (dashed red lines) and the combined JLA + BAO (dotted black lines), and in the Likelihood approach (three right panels), with the JLA only (solid blue lines) and the combined JLA + BAO (solid black lines). The dashed brown lines are the contours for the BAO only.

6. Conclusions

In this paper we have presented exact inhomogeneous LTB models that can suppress the need of dark energy to explain the present acceleration of the universe. Within this scenario, the observational data indicate that we live in a large inhomogeneous void of the order of few Gigaparsec. In particular, we considered three different profiles of void LTB universe models. Both the CGBH and $C\nu$ -ln2 profiles have three cosmological parameters unlike the Gaussian profile that has only two parameters. In order to include the BAO analysis, we have added an extra parameter f_b that represents the Baryon fraction over the total matter content. In addition, there are also the supernovae nuisance parameters in the distance estimate which are the same in all cases.

We performed the best fit analysis and constrained the space of parameters for the inhomogeneous models. This analysis was carried out using BAO and SNIa data separately and also the JLA + BAO combined analysis. We have been careful to calibrate SNIa data specifically for the LTB dynamics. The dependence on the background dynamics does not change significantly from an FLRW background but this calibration is necessary and should be checked every time.

We have also tested the validity of the χ^2 minimization compared to the complete Likelihood approach. Our results corroborate with [51] presenting a specific example where these two approaches are not equivalent. The supernovae parameters (α , β , M_B^1 and Δ_M) have similar results for all cases, but present bias in both approaches. On the other hand, the cosmological parameters ($\Omega_{M,in}$, Δr , ν and r_0) have considerable deviation regardless of the method. For example, the $C\nu$ -ln2 model presents higher matter density $\Omega_{M,in}$ than the CGBH and Gaussian models. The contour levels for the χ^2 and Likelihood approaches display similar shapes and areas but significant bias in the best fit values with the Likelihood contours slightly bigger than the χ^2 .

Figures 8 and 9 show the 1D probability distribution function (PDF) of the σ_{int} parameter for the three models, considering, respectively, only the JLA sample and the JLA + BAO combined analysis. These results also agree with the issues and criticisms related to the χ^2 analysis.

We found a tension between the confidence contours coming separately from SNIa and BAO data. This discrepancy stems from the behaviour of the LTB radial and transverse expansion rates, which works differently for BAO and SNIa. Indeed, the low value of $\Omega_{M\text{in}}$ needed to fit the SNIa data increases the expansion rate that consequently stretches the BAO scale near the center. This discrepancy was seen at more than 3σ in figure 10, for CGBH, and at lower confidence level for Gaussian and $C\nu\text{-ln}2$ models (figures 11 and 12).

Finally, we have analysed the AIC and BIC information criteria in order to evaluate the best model. The Gaussian model is slightly favored in comparison with the CGBH and $C\nu\text{-ln}2$ models. But still the Λ CDM is the best favored. The main difference in the profiles is the number of parameters where the Gaussian profile has one less than the others. This is an advantage in the information criterion and given the proximity of the result it is arguably the reason for it to exceed the other models. We have also calculated an approximate Bayes factor, which when using only SNIa data indicates strong evidence for the Λ CDM model against Gaussian model in contrast with both the CGBH and $C\nu\text{-ln}2$ models that suggests very strong evidence for the Λ CDM model. For the combined BAO + SNIa analysis, the Λ CDM model has very strong evidence against the three LTB models.

Acknowledgments

We acknowledge the Conselho Nacional de Desenvolvimento Científico e Tecnológico (CNPq—Brazil) and the Coordenação de Aperfeiçoamento de Pessoal de Nível Superior (CAPES) for financial support.

References

- [1] Riess A G *et al* 1998 Observational evidence from supernovae for an accelerating universe and a cosmological constant *Astron. J.* **116** 1009
- [2] Perlmutter S *et al* 1999 Measurements of Ω and Λ from 42 high-redshift supernovae *Astrophys. J.* **517** 565
- [3] Spergel D N *et al* 2003 First year Wilkinson microwave anisotropy probe (WMAP) observations: determination of cosmological parameters *Astrophys. J. Suppl.* **148** 175
- [4] Tegmark M *et al* 2004 Cosmological parameters from SDSS and WMAP *Phys. Rev. D* **69** 103501
- [5] Seljak U *et al* 2005 Cosmological parameter analysis including SDSS Ly-alpha forest and galaxy bias: constraints on the primordial spectrum of fluctuations, neutrino mass, and dark energy *Phys. Rev. D* **71** 103515
- [6] Eisenstein D J *et al* 2005 Detection of the baryon acoustic peak in the large-scale correlation function of SDSS luminous red galaxies *Astrophys. J.* **633** 560
- [7] Fu L *et al* 2008 Very weak lensing in the CFHTLS Wide: cosmology from cosmic shear in the linear regime *Astron. Astrophys.* **479** 9
- [8] Buchert T, Coley A A, Kleinert H, Roukema B F and Wiltshire D L 2016 Observational challenges for the standard FLRW model *Int. J. Mod. Phys. D* **25** 1630007
- [9] Bharat R and Peebles P J E 1988 Cosmological consequences of a rolling homogeneous scalar field *Phys. Rev. D* **37** 3406
- [10] Armendariz-Picon C, Mukhanov V and Steinhardt P J 2001 Essentials of k-essence *Phys. Rev. D* **63** 103510
- [11] Campos J P, Fabris J C, Perez R, Piattella O F and Velten H 2013 Does Chaplygin gas have salvation? *Eur. Phys. J. C* **73** 2357

- [12] Miranda V, Jorás S E, Waga I and Quartin M 2009 Viable singularity-free $f(R)$ gravity without a cosmological constant *Phys. Rev. Lett.* **102** 221101
- [13] Zumalacárregui M, Koivisto T S and Mota D F 2013 DBI Galileons in the Einstein frame: local gravity and cosmology *Phys. Rev. D* **87** 083010
- [14] Maier R and Falciano F T 2011 Brane world in non-Riemannian geometry *Phys. Rev. D* **83** 064019
- [15] Clarkson C, Clifton T, Coley A and Sung R 2012 Observational constraints on the averaged universe *Phys. Rev. D* **85** 043506
- [16] Valkenburg W, Marra V and Clarkson C 2014 Testing the Copernican principle by constraining spatial homogeneity *Mon. Not. R. Astron. Soc.* **438** L6
- [17] Mustapha N, Hellaby C and Ellis G F 1997 Large-scale inhomogeneity versus source evolution: can we distinguish them observationally? *Mon. Not. R. Astron. Soc.* **292** 817
- [18] Célérier M 2000 Do we really see a cosmological constant in the supernovae data? *Astron. Astrophys.* **353** 63
- [19] Iguchi H, Nakamura T and Nakao K-I 2002 Is dark energy the only solution to the apparent acceleration of the present universe? *Prog. Theor. Phys.* **108** 809
- [20] Bull P, Clifton T and Ferreira P G 2012 Kinematic Sunyaev–Zel’dovich effect as a test of general radial inhomogeneity in Lemaître–Tolman–Bondi cosmology *Phys. Rev. D* **85** 024002
- [21] Yan X-P, Liu D-Z and Wei H 2015 Age problem in Lemaître–Tolman–Bondi void models *Phys. Lett. B* **742** 149–59
- [22] Sundell P, Mörtzell E and Vilja I 2015 Can a void mimic the Λ in Λ CDM? *J. Cosmol. Astropart. Phys.* **JCAP08(2015)037**
- [23] Célérier M N 2012 Some clarifications about Lemaître–Tolman models of the Universe used to deal with the dark energy problem *Astron. Astrophys.* **543** A71
- [24] Redlich M, Boljko K, Meyer S, Lewis G F and Bartelmann M 2014 Probing spatial homogeneity with LTB models: a detailed discussion *Astron. Astrophys.* **570** A63
- [25] Isidro E G C, Vargas C Z and Zimdahl W 2015 Simple inhomogeneous cosmological (toy) models *J. Cosmol. Astropart. Phys.* **JCAP05(2016)003**
- [26] Betoule M *et al* 2014 Improved cosmological constrain from a joint analysis of the SDSS-II and SNLS supernova samples *Astron. Astrophys.* **568** A22
- [27] Lemaître G 1997 The expanding universe *Gen. Rel. Grav.* **29** 641
- [28] Tolman R C 1934 Effect of inhomogeneity on cosmological models *Proc. Natl Acad. Sci.* **20** 169
- [29] Bondi H 1947 Spherically symmetrical models in general relativity *Mon. Not. R. Astron. Soc.* **107** 410
- [30] Enqvist K and Mattsson T 2007 The effect of inhomogeneous expansion on the supernova observations *J. Cosmol. Astropart. Phys.* **JCAP02(2007)019**
- [31] Enqvist K 2008 Lemaître–Tolman–Bondi model and accelerating expansion *Gen. Rel. Grav.* **40** 451
- [32] Silk J 1977 Large-scale inhomogeneity of the universe—spherically symmetric models *Astron. Astrophys.* **59** 53
- [33] Zibin J P 2008 Scalar perturbations on Lemaître–Tolman–Bondi spacetimes *Phys. Rev. D* **78** 043504
- [34] Etherington I M H 2007 Republication of: LX. On the definition of distance in general relativity *Gen. Rel. Grav.* **39** 1055
- [35] Ellis G F R 2009 Republication of: Relativistic cosmology *Gen. Rel. Grav.* **41** 581
- [36] Garcia-Bellido J and Haugbølle T 2008 Confronting the Lemaître–Tolman–Bondi models with observational cosmology *J. Cosmol. Astropart. Phys.* **JCAP04(2008)003**
- [37] Uzan J-P, Clarkson C and Ellis G 2008 Time drift of cosmological redshifts as a test of the Copernican principle *Phys. Rev. Lett.* **100** 191303
- [38] Yoo C-M, Kai T and Nakao K-I 2011 Redshift drift in Lemaître–Tolman–Bondi void universes *Phys. Rev. D* **83** 043527
- [39] Zumalacárregui M, Garcia-Bellido J and Ruiz-Lapuente P 2012 Tension in the void: cosmic rulers strain inhomogeneous cosmologies *J. Cosmol. Astropart. Phys.* **JCAP10(2012)009**
- [40] Crocce M and Scoccimarro R 2008 Nonlinear evolution of baryon acoustic oscillations *Phys. Rev. D* **77** 023533
- [41] Angulo R, Baugh C M, Frenk C S and Lacey C G 2008 The detectability of baryonic acoustic oscillations in future galaxy surveys *Mon. Not. R. Astron. Soc.* **383** 755
- [42] Smith R E, Scoccimarro R and Sheth R K 2008 Eppur Si muove: on the motion of the acoustic peak in the correlation function *Phys. Rev. D* **77** 043525
- [43] Clarkson C, Clifton T and February S 2009 Perturbation theory in Lemaître–Tolman–Bondi cosmology *J. Cosmol. Astropart. Phys.* **JCAP06(2009)025**

- [44] February S, Clarkson C and Maartens R 2013 Galaxy correlations and the BAO in a void universe: structure formation as a test of the Copernican Principle *J. Cosmol. Astropart. Phys.* [JCAP03\(2013\)023](#)
- [45] Eisenstein D J and Hu W 1998 Baryonic features in the matter transfer function *Astrophys. J.* [496 605](#)
- [46] Okumura T, Matsubara T, Eisenstein D J, Kayo I, Hikage C, Szalay A S and Schneider D P 2008 Large-scale anisotropic correlation function of SDSS luminous red galaxies *Astrophys. J.* [676 889](#)
- [47] Shoji M, Jeong D and Komatsu E 2009 Extracting angular diameter distance and expansion rate of the universe from two-dimensional galaxy power spectrum at high redshifts: baryon acoustic oscillation fitting versus full modeling *Astrophys. J.* [693 1404](#)
- [48] Percival W J *et al* 2010 Baryon acoustic oscillations in the sloan digital sky survey data release 7 galaxy sample *Mon. Not. R. Astron. Soc.* [401 2148](#)
- [49] Biswas T, Notari A and Valkenburg W 2010 Testing the void against cosmological data: fitting CMB, BAO, SN and H0 *J. Cosmol. Astropart. Phys.* [JCAP11\(2010\)030](#)
- [50] Guy J *et al* 2007 SALT2: using distant supernovae to improve the use of type Ia supernovae as distance indicators *Astron. Astrophys.* [466 11](#)
- [51] Lago B L, Calvi M O, Jor S E, Reis R R R, Waga I and Giotri R 2012 Type Ia supernova parameter estimation: a comparison of two approaches using current datasets *Astron. Astrophys.* [546 A110](#)
- [52] Kessler R *et al* 2009 First-year Sloan Digital Sky Survey-II supernova results: Hubble diagram and cosmological parameters *Astrophys. J. Suppl.* [185 32](#)
- [53] Beutler F *et al* 2011 The 6dF galaxy survey: baryon acoustic oscillations and the local Hubble constant *Mon. Not. R. Astron. Soc.* [416 3017](#)
- [54] Padmanabhan N *et al* 2012 A 2 per cent distance to $z = 0.35$ by reconstructing baryon acoustic oscillations I. Methods and application to the Sloan Digital Sky Survey *Mon. Not. R. Astron. Soc.* [427 2132](#)
- [55] Anderson L *et al* 2013 The clustering of galaxies in the SDSS-III baryon oscillation spectroscopic survey: baryon acoustic oscillations in the data release 9 spectroscopic galaxy sample *Mon. Not. R. Astron. Soc.* [427 3435](#)
- [56] Blake C *et al* 2011 The WiggleZ dark energy survey: mapping the distance-redshift relation with baryon acoustic oscillations *Mon. Not. R. Astron. Soc.* [418 1707](#)
- [57] Carnero A *et al* 2012 Clustering of photometric luminous red galaxies II: cosmological implications from the baryon acoustic scale *Mon. Not. R. Astron. Soc.* [419 1689](#)
- [58] Akaike H 1974 A new look at the statistical model identification *IEEE Trans. Autom. Control* [16 716](#)
- [59] Schwarz G 1978 Estimating the dimension of a model *Ann. Stat.* [6 461](#)
- [60] Kass R and Raftery A E 1995 Bayes factors *J. Am. Stat. Assoc.* [90 773–95](#)